RSC Advances

PAPER

View Article Online
View Journal | View Issue

Cite this: *RSC Adv.*, 2014, **4**, 24211

Template-free synthesis of Cu_2O–Co_3O_4 core–shell composites and their application in gas sensing†

Fengdong Qu,[a] Yongfan Wang,[a] Ying Wang,[a] Jingran Zhou*[b] and Shengping Ruan*[a]

Received 12th March 2014
Accepted 13th May 2014

DOI: 10.1039/c4ra02166e

www.rsc.org/advances

Cu_2O–Co_3O_4 core–shell composites were prepared *via* a hydrothermal method. The influences of the molar ratio of Cu/Co and reaction time on the morphology of Cu_2O–Co_3O_4 core–shell composites were studied in detail. A possible mechanism was proposed on the basis of a series of experiments. Furthermore, these core–shell composites were integrated into a sensorial structure, which exhibited excellent ethanol sensing properties. These properties make the Cu_2O–Co_3O_4 core–shell composites good candidates for ethanol detection.

1. Introduction

Metal oxide semiconductor materials have attracted sustained interest due to their fantastic physical, chemical and other properties. Recently, a lot of efforts, including experimental and theoretical, have been made to study these materials.[1–5] It is known that the morphologies and structures of the metal oxide semiconductor materials have significant influence on their electrical, chemical, optical or other properties.[6–8] Thus, synthesizing novel materials with well-shaped morphology and structure is of great significance. Hetero-nanostructure composites exhibit good performance in many fields, such as gas sensing and electrocatalytic materials. Core–shell nanostructure, as one of hetero-nanostructure composites, has already been widely applied due to its satisfactory performances.[9,10] Moreover, the solution phase route, one method to synthesize hetero-nanostructure oxide composites, is considered to be an efficient method for its low cost, environmental friendliness and controllable structure.

In recent years, the application of nanotechnology in the field of chemosensors has increased rapidly, which results in a growing number of related publications.[11,12] A variety of nanomaterials, such as nanoparts and nanorods, have been applied for VOC sensing elements. These nano-sized building blocks provide many merits, including large surface-to-volume ratio and excellent chemical as well as electrical properties.[13,14] Cu_2O and Co_3O_4, as two important semiconductor materials, have already been investigated and applied as gas sensor.[15–18] Many investigations have demonstrated that hierarchical hetero-structural nanomaterials, which are assembled from low dimensional, nano-building blocks, such as 0D nanoparticles, 1D nanowires, nanorods, nanotubes, and 2D nanosheets, exhibit improved gas sensing performance.[19–21] Moreover, to the best of our knowledge, there are few reports on synthesis of hierarchical Cu_2O–Co_3O_4 core–shell structures. Thus, the investigation of synthesis of Cu_2O–Co_3O_4 core–shell composites, as well as their gas sensing properties, has important scientific and practical significance.

In this work, we successfully prepared Cu_2O–Co_3O_4 core–shell composites through a hydrothermal method. As far as we know, such novel Cu_2O–Co_3O_4 composites obtained by such a simple method have rarely been reported. In order to understand the formation mechanism of these composites, a series of experiments were conducted. As a potential application, these core–shell composites were applied to a gas sensor, and they exhibited excellent ethanol gas sensing performance.

2. Experimental section

2.1 Chemicals

$CuSO_4 \cdot 5H_2O$, trisodium citrate, and KOH were purchased from Beijing Chemicals Co., Ltd. (Beijing, China). $CoCl_2 \cdot 6H_2O$ and glycine were purchased from Xilong Chemical Reagent Co. (Guangdong, China). All of these chemicals were analytical grade and used without any further purification.

2.2 Synthesis of Cu_2O–Co_3O_4 core–shell nanoarchitectures

At first, $CuSO_4 \cdot 5H_2O$ (0.5 mmol) was dissolved in a mixture of water (20 ml) and ethanol (13 ml) to form a clear solution, followed by the addition of $CoCl_2 \cdot 6H_2O$ (1 mmol), trisodium citrate (Na_3Cit) (0.10 g), glycine (0.3 mmol), and KOH (3.0 ml, 200 mmol). The mixture was stirred vigorously for 30 min, and

[a]State Key Laboratory on Integrated Optoelectronics, Changchun 130012, PR China. E-mail: ruansp@jlu.edu.cn; Fax: +86-431-85168242; Tel: +86-431-85168242

[b]College of Electronic Science and Engineering, Changchun 130012, PR China. E-mail: jingranzhou@jlu.edu.cn

† Electronic supplementary information (ESI) available. See DOI: 10.1039/c4ra02166e

then transferred to a Teflon-lined stainless-steel autoclave (50 ml capacity). The autoclave was heated and maintained at 180 °C for 10 h, and then cooled to room temperature. The resulting precursor was washed several times and dried in vacuum at 60 °C for 4 h. Then, the obtained powders were calcined in air at 300 °C for 2 h, and Cu_2O–Co_3O_4 core–shell composites were prepared.

2.3 Sample characterization

X-ray diffraction (XRD) analysis was conducted on a Scintag XDS-2000 X-ray diffractometer with Cu Kα radiation ($\lambda = 1.5418$ Å). X-ray photoelectron spectroscopy (XPS) data was obtained with a VG ESCALAB MK II spectrometer with an Mg KR excitation (1253.6 eV). Scanning electron microscopy (SEM) images were performed on a SHIMADZU SSX-550 (Japan) instrument. N_2 adsorption–desorption isotherms were measured at 77 K on a Micromeritics ASAP2000 system. Surface area and pore-size distribution were evaluated using Brunauer–Emmett–Teller (BET) and Barrett–Joyner–Halenda (BJH) methods, respectively (Quantachrome Instruments AUTOSORB-1, Boynton Beach, FL).

2.4 Gas sensor fabrication and response test

The as-prepared sample was mixed with deionized water in a weight ratio of 100 : 25 and ground in a mortar for 3 h to form a paste. The paste was then coated on a ceramic tube to form a sensing film (with a thickness of about 300 μm), on which a pair of Au electrodes was previously printed. Pt lead wires were attached to these electrodes and used as electrical contacts. The morphology (variance), which is produced by the "pasting" technique, is the reason for the different signals obtained from the different sensing results processes, as has been obtained in other (previous) publications.[22–25] After the ceramic tube was calcined at 300 °C for 2 h, a Ni–Cr heating wire was inserted in the tube to control the operating temperature. The structure of the sensor is shown in Fig. 1a. The details of the sensor fabrication were similar to our previous works.[26,27]

Gas sensing properties were measured by a CGS-8 (Chemical gas sensor-8) intelligent gas sensing analysis system (Beijing Elite Tech Co., Ltd., China) (Fig. 1b). The sensors were pre-heated at different operating temperatures for about 30 min. When the resistances of all the sensors were stable, saturated target gas was injected into the test chamber (20 l in volume) by a microinjector through a rubber plug. Our target liquid, *i.e.* ethanol, was injected into the evaporator to form ethanol vapour. The saturated target gas was mixed with air (relative humidity was about 40%, which was measured by a humidity sensor) by two fans in the analysis system. After the sensor resistances reached a new constant value, the test chamber was opened to recover the sensors in air. All the measurements were performed in a laboratory fume hood in a super-clean room. The sensor resistance and response values were acquired by the analysis system automatically. The response value (R) was defined as $R = R_g/R_a$, where R_a and R_g denoted the sensor's resistance in the absence and in the presence of the target gases, respectively. The time taken by the sensor to achieve 90% of the total resistance change was defined as the "response time" in the case of response (target gas adsorption) or the "recovery time" in the case of recovery (target gas desorption).

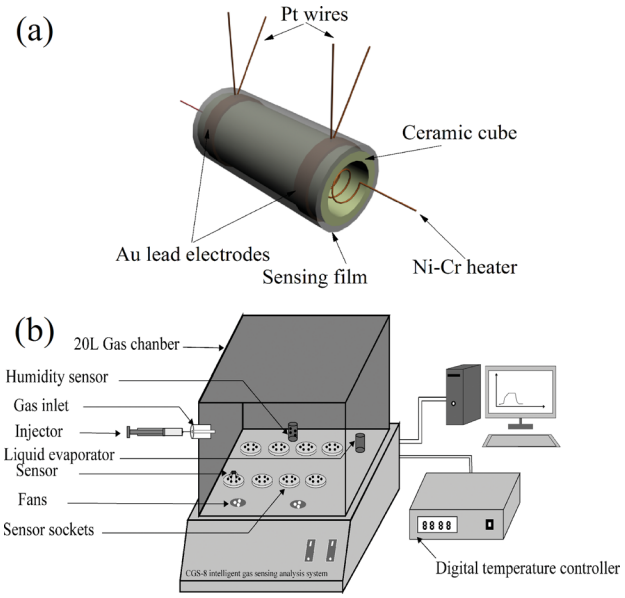

Fig. 1 Schematic illustration of (a) the gas sensor and (b) CGS-8 intelligent gas sensing analysis system.

3. Results and discussion

3.1 Characterization of Cu_2O–Co_3O_4 core–shell composites

The crystal phase of Cu_2O–Co_3O_4 core–shell composites was identified by X-ray powder diffraction (XRD), which was shown in Fig. 2a. The curve exhibited sharp diffraction peaks, which indicated the optimal crystallization of Cu_2O–Co_3O_4 core–shell composites. All the peaks in Fig. 2a can be indexed to Co_3O_4 (JCPDS File no. 42-1467) and Cu_2O (JCPDS File no. 78-2076). There were no other clear sharp peaks coincident with those peaks of other impurities. These results confirmed that Cu_2O–Co_3O_4 core–shell composites with relatively high crystal purity were obtained. Moreover, the XPS peaks were indexed to the composite Cu_2O–Co_3O_4 core–shell nanostructures. The binding energy for the C 1s peak (284.7 eV) was used as an internal reference. As depicted in Fig. 2e, peaks centred at 932.7 eV and 952.6 eV correspond to the Cu $2p_{3/2}$ and Cu $2p_{1/2}$ of Cu_2O composites, respectively.[28] Similarly, the peak centred at 779.8 eV corresponds to Co $2p_{3/2}$ and another one centred at 794.8 eV corresponds to Co $2p_{1/2}$. Note that the energy difference between Co $2p_{3/2}$ and Co $2p_{1/2}$ splitting is 15.0 eV, which indicated the existence of both Co^{2+} and Co^{3+}.[29,30] Moreover, the intensity of Co peaks is higher than that of Cu peak, which possibly confirms that the $2p_{3/2}$ and Co $2p_{1/2}$ splitting was 15.0 eV, thus confirming the hierarchical core–shell structure. In order to confirm the porosities of the product, the BET surface area and the pore-size distribution of the product were determined by measuring the corresponding nitrogen adsorption–desorption isotherms, which are shown in Fig. 2b. It can be observed that at a high relative pressure, the curve exhibits a type IV isotherm with an H3 hysteresis loop according to

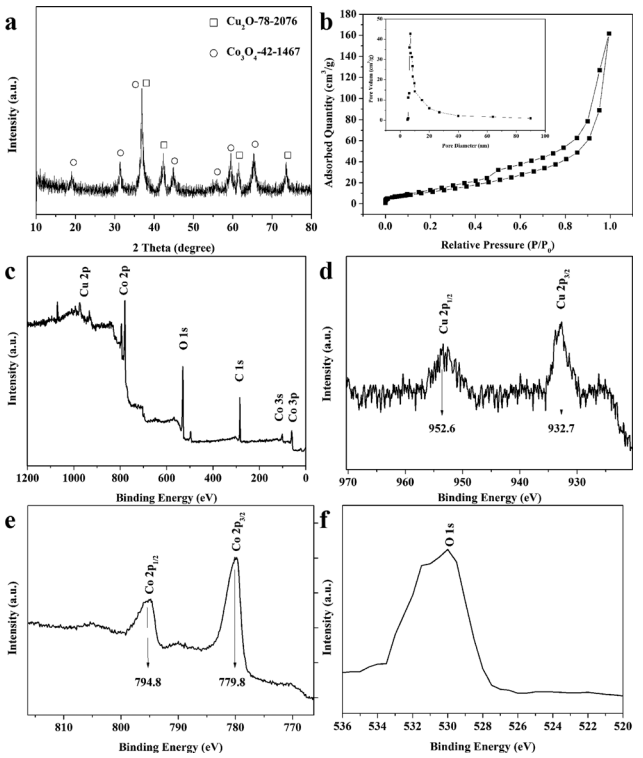

Fig. 2 (a) XRD pattern, (b) typical N_2 adsorption–desorption isotherms and pore-size distribution curve (the inset), (c–f) XPS spectra of Cu_2O–Co_3O_4 core–shell nanostructures: (c) full spectrum; (d) Cu 2p; (e) Co 2p; (f) O 1s.

Brunauer–Deming–Deming–Teller (BDDT) classification, which indicates the presence of slit-like mesopores (2–50 nm) in our sample.[31] The BET surface area of core–shell composites is determined to be 95.1 $m^3\ g^{-1}$. The inset is the pore-size distribution of the composites, and most of the pores fall into the size range of 5–50 nm.

The morphology and structure of the as-prepared products were observed by scanning electron microscopy (SEM). Fig. 3a shows the low-magnification of SEM image of the product, from which we can observe that the products consist of relatively uniform Cu_2O–Co_3O_4 composites with diameters from 600 to 800 nm. The high-magnification SEM images shown in Fig. 3b and c provide detailed information of the product's surface, which is assembled from 2D nanosheets (or 1D nanorods) with a thickness of about 10 nm. Fig. 3d shows the SEM image of a broken single microsphere. It could be observed that the microsphere was assembled from a core and shell, which confirm the core–shell structure of the as-prepared products.

The influence of different molar ratios of Cu/Co on morphology was investigated by varying the molar ratio of Cu/Co (1 : 0, 2 : 1, 1 : 2 and 0 : 1) while keeping the other conditions the same. The SEM images of the products of different molar ratios are shown in Fig. S1.† From Fig. S1,† we can conclude that with the increase of molar ratio of Cu/Co from 1 : 0 to 1 : 2, the petals of the products grew, and the quantity of the as-prepared core–shell products was also increased. The perfect products were obtained at the molar ratio

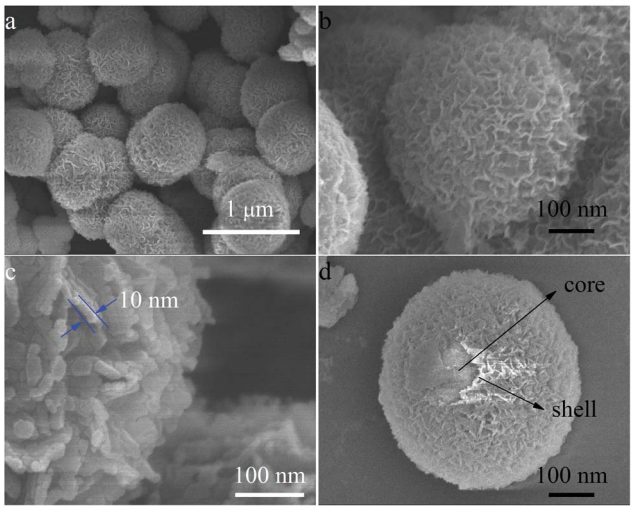

Fig. 3 (a) Low- and (b) high-magnification SEM images of the Cu_2O–Co_3O_4 core–shell nanostructures. (c) High-magnification SEM image of the Co_3O_4 shell. (d) SEM image of a broken Cu_2O–Co_3O_4 core–shell microsphere.

of 1 : 2. When the molar ratio of Cu/Co reaches 0 : 1, there is no core–shell structure observed, which is shown in Fig. S1d.†

In order to study the formation mechanism of the Cu_2O–Co_3O_4 core–shell composites in this work, a series of time-dependent experiments were conducted. Fig. 4a–d exhibited typical results received at 2, 5, 7, 10 h. It was observed that there

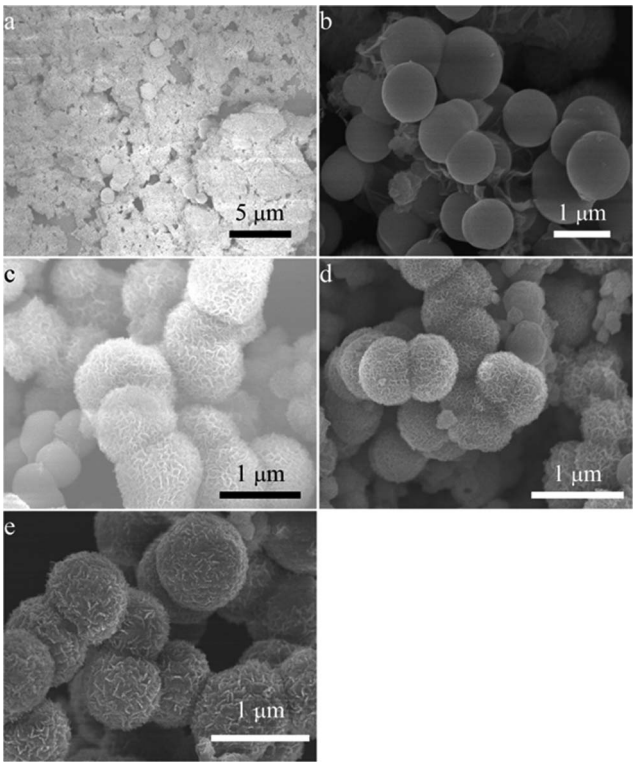

Fig. 4 SEM images of the morphology evolution at different reaction times: (a) 2 h, (b) 5 h, (c) 7 h, and (d) 10 h. (e) SEM image of the products after being calcined at 300 °C for 1 h.

was rarely shaped product after 3 h (Fig. 4a), and when the time is further increased to 5 h, the cores all grew well and some shells appeared, which are shown in Fig. 4b. With a further increase to 7 h, the most basic core–shell structure had already formed, although $Co(OH)_2$ core–shell composites (Fig. 5d) were completely formed. Fig. 4e showed the product (Cu_2O–Co_3O_4 core–shell composites) of the calcined Cu_2O–$Co(OH)_2$ core–shell composites. It could be observed that the surface of Cu_2O–$Co(OH)_2$ core–shell composites became rough after being calcined. In order to prove the components of the products obtained above, the XRD patterns of the products were measured and shown in Fig. S2.†

According to the evidence above, a possible mechanism shown in Fig. 5 may explain the growth of the core–shell composites. Firstly, Cu_2O nanoparticles form in the water, and with the presence of Cit^{3-}, they aggregate together to grow into sphere-like shapes.[32] Thus, Cit^{3-} is adsorbed on the surface of the Cu_2O core. Then, Co^{2+} is absorbed by Cu_2O cores, because Co^{2+} can chelate with Cit^{3-}. With increase in time, the $Co(OH)_2$ nanosheets form on the surface of the Cu_2O cores and the shell eventually forms. After being calcined, the Cu_2O–$Co(OH)_2$ core–shell composites transfer to Cu_2O–Co_3O_4 composites. The detailed mechanism for the formation of porous Cu_2O–Co_3O_4 core–shell flower-like structures is still under investigation by our group. Herein is a working hypothesis that agreed well with the electron microscopy and XRD pattern of the obtained products.

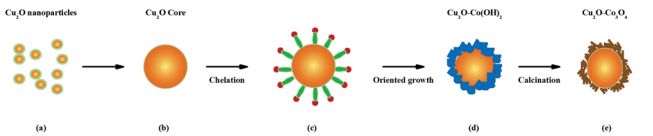

Fig. 5 Schematic illustration of the formation process of the hierarchical Cu_2O–Co_3O_4 core–shell nanostructures.

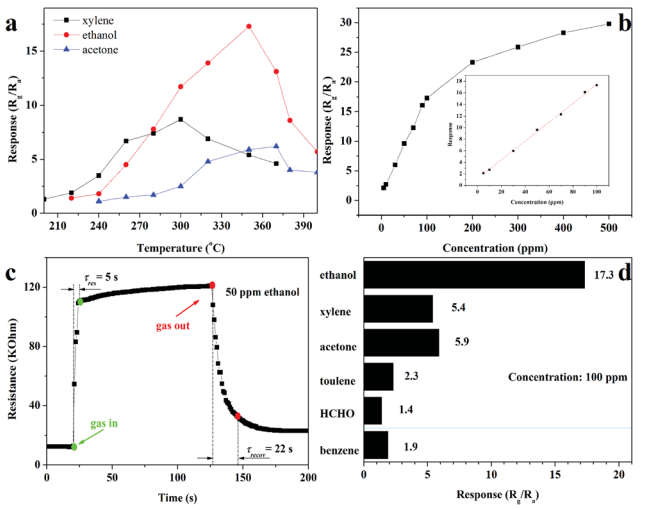

Fig. 6 (a) Response of sensor, based on the as-prepared core–shell nanoarchitecture, to 100 ppm xylene, ethanol and acetone as a function of the operating temperature. (b) Response of the sensor *versus* different ethanol concentrations at 350 °C (the inset shows the corresponding response *versus* the concentrations from 5–100 ppm). (c) Response transients of the sensor to 50 ppm ethanol gas at 350 °C, τ_{res} and τ_{recov} stand for the response time and recovery time, respectively. (d) Response of sensor based on hierarchical Cu_2O–Co_3O_4 core–shell nanostructure to 100 ppm various gases at 350 °C.

3.2 Gas sensing properties

In order to evaluate the optimum operating temperature for Cu_2O–Co_3O_4 core–shell composites, different tests were measured for different target gases. The gas sensor response was collected upon exposure to different target gases under dry air for the operating temperatures from 200 to 400 °C. Fig. 6a shows the sensor responses values as a function of operating temperature for 100 ppm ethanol, acetone and xylene. It was observed that the responses of the tested sensor varied with operating temperature. According to Fig. 6a, 300, 350 and 370 °C were suggested to be the optimum operating temperature for xylene, ethanol and acetone detection, respectively. The maximum response of the sensor to 100 ppm xylene, ethanol and acetone reached 8.7, 17.3 and 6.2. The variation in the optimum operating temperatures for xylene, ethanol and acetone could be understood by the dynamic equilibrium state of the initial adsorption and the subsequent desorption of the gases.[33]

Fig. 6b shows the responses of the sensor *versus* different ethanol concentration at 350 °C. According to the curve, we can

Table 1 Response and recovery time of the Cu_2O–Co_3O_4 core–shell composites sensor to various concentrations of ethanol at 350 °C

Ethanol conc. (ppm)	Response time (s)	Recovery time (s)
5	5	10
50	5	22
100	13	35
200	18	41
500	20	44

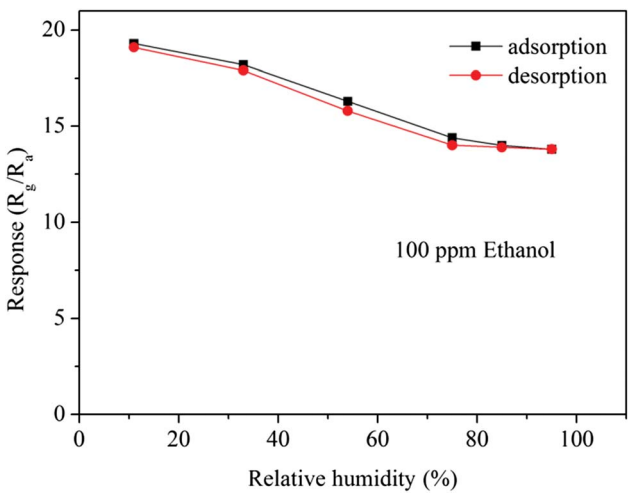

Fig. 7 Humidity hysteresis characteristics of the sensor based on Cu_2O–Co_3O_4 core–shell composites.

Table 2 Comparison of gas-sensing characteristics of the as-prepared ethanol sensors with other ethanol gas sensor

Materials	Ethanol conc. (ppm)	Response	Response time (s)	Reference
Cu_2O–Co_3O_4 composites	100	17.3	13	This work
Porous Co_3O_4 microspheres	100	10.5	—	17
Au-supported Cu_2O nanocubes	100	4.34	6	36
α-Fe_2O_3/ZnO heterostructures	100	13.0	20	37
Commercial ethanol sensor	100	10	—	TGS2620 (Figaro Engineering Inc., Japan)

observe that the response increased with increase in the ethanol concentration from 5 to 500 ppm. When the concentration was below 100 ppm, the response increased relatively fast. When the concentration reached 100 ppm, with a further increase of the ethanol concentration, the response of the sensor gradually tended to saturation. A linear relationship ($y = 0.16256x + 1.19849$) between the response and ethanol concentration was observed in range of 5–100 ppm. The detection limit of ethanol for the sensor based on the as-prepared Cu_2O–Co_3O_4 core–shell composites was estimated to be approximately 92 ppb, when the criterion for gas detection was set to $R_g/R_a > 1.2$.

Fig. 6c shows the response behaviour and recovery behavior of the sensor exposed to 50 ppm ethanol at 350 °C. From the curve, we could read out that the response time (τ_{res}) and the recovery time (τ_{recov}) were 5 and 22 s, respectively. The τ_{res} and τ_{recov} of other ethanol concentrations are shown in Table 1. The responses of the sensor based on Cu_2O–Co_3O_4 core–shell composites to different VOC gases (100 ppm) were measured at the operating temperature of 350 °C, which is shown in Fig. 6d. The result showed that the sensor had an obvious response to ethanol, and less effective response to other tested gases. This indicated that the sensor exhibited excellent ethanol gas sensing properties, which may have excellent selectivity by ANN models.[11,34]

It is known that the hysteresis effect (if large), would mask or cause "artifacts."[35] Thus, we checked the influence of hysteresis effect on our sensor's gas sensing properties, which is shown Fig. 7. It can be observed that the sensor's response to 100 ppm ethanol decreases with the humidity increasing from 11 to 95% RH (adsorption process). When the humidity decreases from 95 to 11% RH (desorption progress), the sensor's response increases. The maximum hysteresis value is less than 5% RH, indicating that the hysteresis effect of the sensor was not too large to influence the application in real-world conditions.

A comparison between the sensing performances of the sensor and literature reports is summarized in Table 2. To date, many studies have reported ethanol gas sensing properties. It is noteworthy that the sensor fabricated in our work exhibits better sensing performance compared with those reported in the literatures and the commercial ethanol sensor (TGS2620, Figaro Engineering Inc., Japan).[17,36,37]

4. Conclusion

In summary, we reported the synthesis of Cu_2O–Co_3O_4 core–shell composites *via* a hydrothermal method and investigated their ethanol sensing properties. A possible mechanism was proposed on the basis of a series of experiments. An excellent ethanol sensing property was observed. The excellent gas sensing properties can be probably attributed to the synergetic effect of Cu_2O and Co_3O_4, as well as the assembled heterojunction. The results demonstrate that the hierarchical core–shell nanostructure sensor is a potential candidate for high performance ethanol gas sensors.

Acknowledgements

This work was supported by the National Natural Science Foundation of China (Grant no. 61274068, and 61275035), Chinese National Programs for High Technology Research and Development (Grant no. 2013AA030902), Project of Science and Technology Development Plan of Jilin Province (Grant no. 20120324, and 20130206021GX), and the Opened Fund of the State Key Laboratory on Integrated Optoelectronics (no. IOSKL2012KF03).

Notes and references

1 J. Elias, C. Lévy-Clément, M. Bechelany, J. Michler, G.-Y. Wang, Z. Wang and L. Philippe, *Adv. Mater.*, 2010, **22**, 1607–1612.
2 J. Liu, J. Jiang, C. Cheng, H. Li, J. Zhang, H. Gong and H. J. Fan, *Adv. Mater.*, 2011, **23**, 2076–2081.
3 H. Zhang, R. Wu, Z. Chen, G. Liu, Z. Zhang and Z. Jiao, *CrystEngComm*, 2012, **14**, 1775–1782.
4 X. Liu, J. Zhang, Y. Kang, S. Wu and S. Wang, *CrystEngComm*, 2012, **14**, 620–625.
5 X. Xiao, X. Liu, H. Zhao, D. Chen, F. Liu, J. Xiang, Z. Hu and Y. Li, *Adv. Mater.*, 2012, **24**, 5762–5766.
6 A. Gurlo, *Nanoscale*, 2011, **3**, 154–165.
7 M. S. Lord, M. Foss and F. Besenbacher, *Nano Today*, 2010, **5**, 66–78.
8 H. N. Tsao, D. Cho, J. W. Andreasen, A. Rouhanipour, D. W. Breiby, W. Pisula and K. Müllen, *Adv. Mater.*, 2009, **21**, 209–212.
9 S. Zhang, J. Li, T. Wen, J. Xu and X. Wang, *RSC Adv.*, 2013, **3**, 2754–2764.
10 C. Locatelli, A. Minguzzi, A. Vertova and S. Rondinini, *J. Appl. Electrochem.*, 2013, **43**, 171–179.
11 G. Konvalina and H. Haick, *Acc. Chem. Res.*, 2014, **47**, 66–76.

12 H. Haick, Y. Y. Broza, P. Mochalski, V. Ruzsanyi and A. Amann, *Chem. Soc. Rev.*, 2014, **43**, 1423–1449.
13 Y. Y. Broza and H. Haick, *Nanomedicine*, 2013, **8**, 785–806.
14 Y. Paska, T. Stelzner, S. Christiansen and H. Haick, *ACS Nano*, 2011, **5**, 5620–5626.
15 L. Guan, H. Pang, J. Wang, Q. Lu, J. Yin and F. Gao, *Chem. Commun.*, 2010, **46**, 7022–7024.
16 S. Deng, V. Tjoa, H. M. Fan, H. R. Tan, D. C. Sayle, M. Olivo, S. Mhaisalkar, J. Wei and C. H. Sow, *J. Am. Chem. Soc.*, 2012, **134**, 4905–4917.
17 C. Sun, S. Rajasekhara, Y. Chen and J. B. Goodenough, *Chem. Commun.*, 2011, **47**, 12852–12854.
18 B. Geng, F. Zhan, C. Fang and N. Yu, *J. Mater. Chem.*, 2008, **18**, 4977–4984.
19 C. C. Li, X. M. Yin, Q. H. Li and T. H. Wang, *CrystEngComm*, 2011, **13**, 1557–1563.
20 W. Zeng, T. Liu and Z. Wang, *J. Mater. Chem.*, 2012, **22**, 3544–3548.
21 S. Zhang, F. Ren, W. Wu, J. Zhou, X. Xiao, L. Sun, Y. Liu and C. Jiang, *Phys. Chem. Chem. Phys.*, 2013, **15**, 8228–8236.
22 M. Segev-Bar, G. Shuster and H. Haick, *J. Phys. Chem. C*, 2012, **116**, 15361–15368.
23 Y. Zilberman, U. Tisch, G. Shuster, W. Pisula, X. Feng, K. Müllen and H. Haick, *Adv. Mater.*, 2010, **22**, 4317–4320.
24 N. Gozlan, U. Tisch and H. Haick, *J. Phys. Chem. C*, 2008, **112**, 12988–12992.
25 N. Gozlan and H. Haick, *J. Phys. Chem. C*, 2008, **112**, 12599–12601.
26 C. Feng, W. Li, C. Li, L. Zhu, H. Zhang, Y. Zhang, S. Ruan, W. Chen and L. Yu, *Sens. Actuators, B*, 2012, **166–167**, 83–88.
27 W. Li, C. Li, L. Zhu, C. Feng, W. Chen, W. Guo and S. Ruan, *Integr. Ferroelectr.*, 2012, **138**, 71–76.
28 L. Li, C. Nan, Q. Peng and Y. Li, *Chem.–Eur. J.*, 2012, **18**, 10491–10496.
29 J. Xu, P. Gao and T. S. Zhao, *Energy Environ. Sci.*, 2012, **5**, 5333–5339.
30 J. Yang, H. Liu, W. N. Martens and R. L. Frost, *J. Phys. Chem. C*, 2010, **114**, 111–119.
31 F. Qu, C. Feng, C. Li, W. Li, S. Wen, S. Ruan and H. Zhang, *Int. J. Appl. Ceram. Technol.*, 2013, 1–7.
32 T. Togashi, H. Hitaka, S. Ohara, T. Naka, S. Takami and T. Adschiri, *Mater. Lett.*, 2010, **64**, 1049–1051.
33 Z. Wen and L. Tian-mo, *Phys. B*, 2010, **405**, 1345–1348.
34 B. Wang, J. C. Cancilla, J. S. Torrecilla and H. Haick, *Nano Lett.*, 2014, **14**, 933–938.
35 Y. Paska and H. Haick, *ACS Appl. Mater. Interfaces*, 2012, **4**, 2604–2617.
36 Y. Sui, Y. Zeng, L. Fu, W. Zheng, D. Li, B. Liu and B. Zou, *RSC Adv.*, 2013, **3**, 18651–18660.
37 C. L. Zhu, Y. J. Chen, R. X. Wang, L. J. Wang, M. S. Cao and X. L. Shi, *Sens. Actuators, B*, 2009, **140**, 185–189.

